Self-assembly of flexible and rigid structures: from colloidal molecules to lattices

Shelke, Y.P.

Chapter 3

Flexible Colloidal Molecules with Controlled Flexibility

Abstract

Colloidal molecules are ideal model systems for mimicking real molecules and can serve as versatile building blocks for the bottom-up self-assembly of flexible and smart materials. While most colloidal molecules are rigid objects, the development of colloidal joints has made it possible to endow them with conformational flexibility. However, their unrestricted range of motion does not capture the restricted motion range and bond directionality that is typical of real molecules. In this work, we create flexible colloidal molecules with an *in situ* controllable motion range and bond directionality by assembling spherical particles onto cubes functionalized with complementary surface-mobile DNA. By varying the sphere-to-cube size ratio, we obtain colloidal molecules with different coordination numbers and find that they feature a constrained range of motion above a critical size ratio. Using theory and simulations, we show that the particle shape together with the multivalent bonds create an effective free-energy landscape for the motion of the sphere on the surface of the cube. We quantify the confinement of the spheres on the surface of the cube and the probability to change facet. We find that temperature can be used as an extra control parameter to switch *in situ* between full and constrained flexibility of these colloidal molecules. These flexible colloidal molecules with temperature switching motion range can be used to investigate the effect of directional, yet flexible bonds in determining their self-assembly and phase behavior, and may be employed as constructional units in microrobotics and smart materials.

This chapter is based on:

Yogesh Shelke, Fabrizio Camerin, Susana Marín-Aguilar, Ruben W. Verweij, Marjolein Dijkstra, and Daniela J. Kraft. Flexible colloidal molecules with directional bonds and controlled flexibility. *ACS Nano*, 17(13):12234–12246, 2023.

3.1 Introduction

Colloidal molecules are excellent models for real molecules and can be used to study the influence of shape and bond directionality in self-assembly processes, phase behavior and the creation of colloidal materials.[1–8] However, current colloidal molecules are often rigid objects, while the functionality of many molecules such as polymers, intrinsically disordered proteins, and tRNA hinges on their ability to adapt their structure. This conformational flexibility enables lock-and-key interactions, as well as faster and more specific binding, and has been proposed to affect their diffusive motion.[9–12]

The development of colloidal joints has recently made the fabrication of flexible colloidal molecules through self-assembly possible. These consist of solid particles or liquid droplets that can bind particles such that they can still laterally move on their surface.[13–17] Their intrinsic bond flexibility has been shown to enhance yields in self-assembly.[18] Furthermore, flexible colloidal molecules have been used to demonstrate that flexibility enhances diffusion[19] and that flexible linear and ring-like structures follow Flory theory for polymers.[15, 20, 21] Besides, they have great potential for fundamental studies of their phase behavior, to understand and fabricate reconfigurable materials,[22, 23] and to store information. [24]

However, current realizations of flexible colloidal molecules exclusively feature bonds with an unrestricted range of motion, whereas the bonds of real molecules are often constrained to a specific range of motion due to the orbitals underlying their intramolecular bonds. The restricted motion range thus provides molecules with bond directionality. These features have not been realized in colloidal molecules yet, but would be powerful not only in view of their ability to serve as model systems but also to create reconfigurable materials and functional devices with multiple stable configurations. So far, only a combination of gravitational confinement and steric hindrance of the bound particles could keep their positional order unchanged, but could not confine their motion.[18]

Here, we experimentally realize flexible colloidal molecules with controlled flexibility and directionality by exploiting solid colloidal joints with an anisotropic particle shape. We demonstrate the creation of flexible colloidal molecules with directional bonds and controlled flexibility by mixing colloidal cubes equipped with surface mobile DNA-linkers[13, 14, 16] with an excess number of spheres functionalized with complementary strands. The assembled colloidal molecules consist of cubes surrounded by spheres connected with multivalent bonds of DNA linkers. The anisotropic particle shape is the key ingredient because it guides the position and controls the number of attached particles. Furthermore, the cubic particle shape constrains the lateral motion of the attached particles due to an interplay between the spatially extended multivalent bond formed between the particles and the curvature of the cube, thereby realizing controlled flexibility. We show both by experiments and simulations that the combination of the cubic shape and DNA-mediated bonding provides confinement of the outer particles above a critical size ratio of sphere-to-cube diameter. We justify the observed behavior by calculating the free energy of the spheres experienced at different locations on the surface of the cube based on a theoretical framework that accounts microscopically for the bond formation of surface mobile DNA linkers.[25, 26]

The sensitivity of the DNA-based bonds to temperature allows us to lift confinement of the spheres to the cube sides *in situ* by a simple elevation of temperature. Small colloidal molecules with controlled flexibility and directionality can be separated using a magnet due to the permanent magnetic dipole moment of the hematite cube, providing an easy and efficient means for their exploitation. The features of bond directionality and temperature-controlled switch from limited to full flexibility make these colloidal molecules excellent model systems for studying the phase behavior of molecules and building blocks. This would also enable the assembly of reconfigurable structures with multiple stable configurations, a key ingredient for creating functional devices and machines.

3.2 Materials and Methods

3.2.1 Experimental Section

Materials

Silica microspheres of diameters 0.97±0.05 μm, 1.25±0.05 μm, 1.55±0.05 μm, 2.06±0.05 μm, 3.32±0.05μm and 4.62±0.05 μm in 5 wt/v% suspension were purchased from Microparticles GmbH. Silica particles of diameter 0.66±0.01 μm were synthesized by a Stöber method. Sodium chloride, Ethanol, Sodium hydroxide, Ammoniun hydroxide (28-30 v/v%), Iron(III) Chloride Hexahydrate ($FeCl_3 \cdot 6H_2O$), Tetraethyl orthosilicate (TEOS), 4-(2-hydroxyethyl)-1-piperazineethanesulfonic acid (HEPES), trimethoxysilyl propyl methacrylate (TPM), were purchased from Sigma-Aldrich. 1,2-dioleoyl-*sn*-glycero-3-phosphocholine (DOPC), 1,2-dioleoyl-*sn*-glycero-3-phosphoethanolamine-N--[methoxy(polyethylene glycol)-2000] (DOPE-PEG2000), 1,2-dioleoyl-*sn*-glycero-3-pho-sphoethanolamine-N-(lissamine rhodamine B sulfonyl) (DOPE-Rhodamine) and dye 23-(dipyrrometheneboron difluoride)-24-norcholesterol (TopFluor-Cholesterol) were obtained from Avanti Polar Lipids, Inc.. We used Milli-Q water for all experiments. DNA strands were purchased from Eurogentec. The sequences of DNA used were:
Strand A: Double Stearyl-HEG-5′-TT-TAT-CGC-TAC-CCT–TCG-CAC-AGT-CAC-CTT-CGC-ACA-GTC-ACA-TTC-AGA-GAG-CCC-TGT-CTA-GAG-AGC-CCT–GCC-TTA-CGA-*GTA-GAA-GTA-GG-3′-6FAM*,
Strand B: Double Stearyl-HEG-5′-TT-TAT-CGC-TAC-CCT–TCG-CAC-AGT-CAC-CTT-CGC-ACA-GTC-ACA–TTC-AGA-GAG-CCC-TGT-CTA-GAG-AGC-CCT–GCC-TTA-CGA-*CCT-ACT-TCT-AC-3′-Cy3*,
Strand C: 5′-TCG-TAA-GGC-AGG-GCT-CTC-TAG-ACA-GGG–CTC-TCT-GAA-TGT-GAC-TGT-GCG-AAG-GTG–ACT-GTG-CGA-AGG-GTA-GCG-ATT-TT-3′,
Strand D: Double Stearyl-5TT-TAT-CGC-TAC-CCT-TCG-CAC-AGT-CAA-TCT-AGA-GAG-CCC-TGC-CTT-ACG-A and Strand E: TCG-TAA-GGC-AGG-GCT-CTC-TAG-ATT-GAC-TGT-GCG-AAG-GGT-AGC-GAT-TTT. The linker sequence in strand A and strand B is italicized.

Synthesis of Silica Cubes with Hematite Core

The hematite cubes of edge length 0.83 μm were synthesized following reference[27] and coated with 0.105 μm silica layer using the process described.[28] In a typical synthesis of hematite cubes, 100 ml of aqueous 2M $FeCl_3 \cdot 6H_2O$ was prepared in a 500 ml Pyrex bottle. Next, 100 ml of 5M NaOH solution were added while stirring for 20 seconds. Then, the mixture was stirred continuously for another 10 minutes and subsequently placed in a preheated oven and left undisturbed at 100 °C for 8 days. The resulting hematite cubes were washed several times using centrifugation and redispersed in milliQ water. To coat them with a thin layer of silica, 100 ml of ethanol and 0.6 g of synthesized cubes were mixed under sonication and mechanical stirring in a 2-neck round bottom flask at 50 °C. Subsequently, 5 ml of water, 15 ml of ammonium hydroxide solution and Tetraethyl orthosilicate (TEOS) were poured into the reaction flask. Next, the silica layer was allowed to grow on the cubes surface for 5h. The resulting particles were first washed with ethanol and then with water to remove unreacted chemicals by repeated centrifugation and redispersion.

Preparation of Small Unilamellar Vesicles (SUVs)

Small unilamellar vesicles (SUVs) were prepared using a protocol described in reference.[16] For the preparation of SUVs, we used 77 μl of 25 g/L DOPC, 7.34 μl of 10 g/L DOPE PEG 2000, and 2 μl of either 1 g/L dye DOPE-rhodamine or 2 μl of 1 g/L TopFluor-Cholesterol dissolved in chloroform were mixed together in glass vial. Subsequently, the lipid mixture was dried for at least 2 hrs in the desiccator (Kartell) attached with vacuum pump (KNF LABOPORT N816.3KT.18). Then, 1ml of buffer solution consisting of 50 mM NaCl and 10 mM HEPES at pH 7.4 was added to the dried lipid. The prepared solution was vortexed for 30 min during which the solution became turbid indicating the formation of giant multilamellar vesicles. The dispersion of giant multilamellar vesicles was extruded (Avanti Polar Lipids mini extruder) 21 times through a 50 nm polycarbonate membrane supported with filter paper to achieve SUV formation. The prepared SUVs were stored in the fridge at 4 °C and used for up to 3 days.

DNA Hybridization

We used DNA strands with a hybridized backbone and a single stranded end (linker) and inert double-stranded DNA strands for bonding and stabilizing the colloids, respectively. Prior to use, single strand DNA was hybridized with the complementary backbone. Strand A was hybridized with strand C to yield double-stranded linker DNA , strand B with strand C to obtain complementary double-stranded linker DNA, and strand D with strand E to create double-stranded inert DNA (DNA strands are listed in the materials section). For hybridization, we typically mixed 10 μl of 20 μM single strands and 10 μl of 20 μM complementary backbone in 90 μl buffer (200mM NaCl, 10mM HEPES, at pH 7.4) solution. The DNA solutions were placed in a preheated oven at 94 °C for 30 minutes. The oven then was switched off and allowed to cool slowly overnight. After cooling, the hybridized DNA strands were stored at 4 °C and used for up to 2 months.

Functionalization of Colloidal Particles with a Lipid Bilayer Containing Linker and Inert DNA

To coat particles with a lipid bilayer we used a 25:1 surface ratio of SUVs to particles. We maintained the same surface area ratio of SUVs to particles when coating differently sized particles. Typically, for 1μm particles, we use 100 μl of 0.25 wt/v% particles in Milli-Q water and mixed them with 48 μm 0.5 g/L SUVs. Then, the dispersion was rotated at 8 rpm for 1h. During this period, SUVs collide, burst, spread and form a bilayer on the particles' surface. Then, the coated particles were centrifuged at 800 rpm for 2-5 min and the supernatant containing excess SUVs was removed using a micropipette. Subsequently, a concentration of 300 linker DNA strands/μm^2 surface area was added to the spheres and 2×10^4 strands/μm^2 to the cubes. 1×10^5 strands/μm^2 of inert DNA was added to both particle suspensions. The suspensions were rotated for another 1h. Thereafter, each suspension was centrifuged and washed 2 times with a 50 mM NaCl buffer and then once with 200 mM NaCl buffer. The final suspension it was used in self-assembly experiments.

Sample Preparation, Magnetic Separation and Imaging

For all self-assembly experiments, a sphere-to-cube number ratio of 20:1 was maintained. In a 1.5 ml vial, 50 μl of functionalized 1 μm spherical particles and 2.5 μl of cubic particles were combined with 500 μl of buffer 2 solution. The mixture was then transferred to a customized sample holder and allowed to self-assemble for 12 h. Polyacrylamide (PAA) coated coverslips were used as a substrate. The coverslips were coated with PAA by adapting the protocol in reference.[19]

For magnetic separation of the colloidal molecules after assembly, the sample holder was turned upside down to distribute the particles and colloidal molecules in 3D. Subsequently, a magnet was placed at the bottom of the sample holder to attract the flexible colloidal molecules while the non-magnetic excess spheres remained suspended in the sample. After 5 minutes, the supernatant containing the excess spheres was removed using a micropipette and the sample was resuspended in 200mM NaCl buffer solution. The same procedure was repeated one more time to further remove unbound spheres.

To study how the conformational flexibility of the colloidal molecules changes with temperature, self-assembled $\alpha = 0.93$ flexible colloidal molecules were deposited on coverslip with a damadged PAA coating. The PAA coating on the coverslip partially removed by scratching it with a fine needle. The sample was then placed on a custem-made microscpe stage attached with heating and cooling water circulater (JULABO DYNEO DD-300F) and temperature was monitored in the sample. The sample was heated in 1 °C steps and allowed to equilibrate for 10 min for each step during heating cycle and cooled linearly by circulating water through microscope stage.

Images and videos were captured with a Nikon inverted TI-E microscope equipped with an A1 confocal scan head and a brightfield mode equipped with Prime BSI Express camera (Teledyne Photometrics). The images were taken using with 100x oil objective (N.A. 1.4) at frame rates of up to 25 fps.

3.2.2 Numerical Section

System details

The rounded cube belongs to the family of shapes known as superballs,[29] which interpolate between spheres and cubes. The shape of the superball is described by the equation

$$|x|^n + |y|^n + |z|^n = |r_c|^n = \left|\frac{\sigma_c}{2}\right|^n, \tag{3.1}$$

where n determines the degree of roundness of the superball, while σ_c represents the side length of the superball, which is also used as the unit of length in our modeling and simulations. Comparing with the experimental size, we find that $\sigma_c = 1.04\mu$m. We fix $n = 6$ to roughly capture the shape of the hematite cubes, while varying n from 2 to infinity would produce all intermediate shapes between a sphere and a cube with sharp edges and corners.

We keep the size of the superball fixed and vary the size ratio $\alpha = \sigma_s/\sigma_c$ from 0.63 to 4.44. In all cases, we ensure that the magnitude of the normal vector connecting the surface of the cube to the center of the sphere is $|\vec{n}| = r_s + l = \alpha\sigma_c + l$, where $l = 0.025\sigma$. Following reference.[30, 31] and using Eq. 3.1, we calculate the Gaussian curvature at different positions on the surface of a superball. The positions of the sphere on the superball are limited to ≈ 60000 discrete grid points, for which we compute the free energy. Figure 3.1 illustrates a schematic of the model.

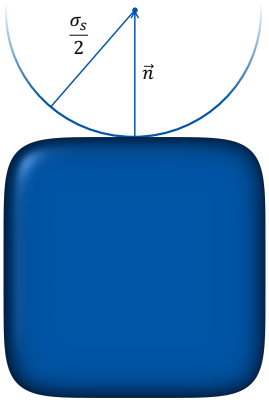

Figure 3.1: Schematics illustrating the numerical model, which consists of spheres of size σ_s moving on the surface of a rounded cube of size σ_c whose shape can be described as a superball. The normal vector $\vec{n}$ connects the center of the sphere to the surface of the rounded cube.

Temperature [$^\circ C$]	NN[32] [kcal/mol]	Salt correction [kcal/mol]	Inert tail correction [kcal/mol]	ΔG_0 [kcal/mol]	ΔG_0 [k_BT]
24	-14.00	1.83	0.34	-11.83	-19.97
36	-11.39	1.83	0.34	-9.22	-15.56
40	-10.52	1.83	0.34	-8.35	-10.56

Table 3.1: Contributions to ΔG_0 for three temperatures.

3.2.3 Free Energy Calculation

Here, we provide a detailed description of the calculation of the free energy associated with the assembly of spherical colloids on the surface of a rounded cube coated with mobile DNA strands.

Attractive free energy for a pair of DNA strands

In this section, we describe the calculation of the attractive part of the free energy for a system consisting of a sphere and a superball. The theoretical treatment is inspired and adapted from reference[25]. As with other models for DNA-mediated assemblies, the first step is to quantify the contributions to the free energy of *single strands* in their hybridized and unhybridized states, thus providing an estimation of the bond energy $\beta\Delta G_{\gamma\delta}$ due to the linking of two complementary strands, denoted as γ and δ. This can be expressed as:

$$\beta\Delta G_{\gamma\delta} = \beta\Delta G_0 + \beta\Delta G_{cnf}, \tag{3.2}$$

where the first term ΔG_0 corresponds to the hybridization energy, which depends solely on the DNA sequence and the salt concentration in the experiments. To calculate this term, we consider the complementary ssDNA end (5'-GTAGAAGTAGG-3' and its complementary sequence), as defined in the Methods section. We calculate ΔG_0 using the nearest-neighbor (NN) SantaLucia approximation,[32] with a salt concentration correction corresponding to 200 mM NaCl and the inert tail correction due to 77 bp of the dsDNA.[33] A summary of each contribution to ΔG_0 is given in Table 3.1.

The second term in Eq. 3.13 can be interpreted as a penalty in configurational entropy, as the hybridized strands are constrained to a smaller configurational space compared to their unhybridized state.[34–36] It can be written as

$$\beta\Delta G_{cnf} = -\ln\left(\frac{1}{\rho_0}\frac{\Omega_{\gamma\delta}}{\Omega_\gamma\Omega_\delta}\right), \tag{3.3}$$

where $\rho_0 = 1\text{M} = 6.76\times10^8\sigma_c^{-3}$ is a standard concentration, $\Omega_{\gamma(\delta)}$ is the configurational space available for a strand $\gamma(\delta)$ when unhybridized and located on a sphere (cube), and $\Omega_{\gamma\delta}$ is the corresponding space for a pair of hybridized strands. $\Omega_{\gamma(\delta)}$

and $\Omega_{\gamma\delta}$ have units of σ_c^3. A common approximation in this context is to treat the strands as rigid rods with an attractive tip,[37] as the dsDNA is smaller than the DNA persistence length at all temperatures investigated,[38] and the interacting ssDNA is smaller than the dsDNA. Depending on the geometry in which the strands are anchored, $\Omega_{\gamma(\delta)}$ can be calculated analytically. In the case of immobile linkers, the available volume accessible to the DNA strands is typically limited to a hemisphere around the point where the linker is attached to the surface.[34] However, for mobile linkers, the volume accessible to the DNA is enlarged due to the freedom of the strands to move on the entire surface of the colloid to which they are attached. Specifically, the DNA strands can explore the volume of a shell of width l around the surface onto which they are bound, where l is the length of the linker. The available space will differ depending on whether the DNA is located on the sphere or on the superball surface. Furthermore, if both particles are within interacting distance, the excluded volume due to both particles must be considered.

For strands located *on the surface of a sphere* with radius $r_s = \sigma_s/2 = \alpha\sigma_c/2$, in the case that the sphere and the superball are at large distances from each other, the available configuration space Ω_γ corresponds to the volume of the spherical shell V_s^{tot}, which is obtained by taking the difference in volume between a sphere of radius $r_{s+l} = \alpha\sigma_c/2 + l$ and a sphere of radius $r_s = \alpha\sigma_c/2$ (see Figure 3.2a):

$$\Omega_\gamma = V_s^{tot} = V_s(\alpha\sigma_c/2 + l) - V_s(\alpha\sigma_c/2), \tag{3.4}$$

where $V_s(r)$ is the volume of a sphere with radius r. Instead, in case the particles are at interacting distance, the volume inaccessible due to steric hindrance needs to be subtracted from V_s^{tot}. This excluded volume is shown in Figure 3.2(c) as the red region, while Ω_γ corresponds to the green region. Hence, we have:

$$\Omega_\gamma = V_s^{tot} - V_{over}(c, s + l), \tag{3.5}$$

where $V_{over}(c, s + l)$ is the volume of overlap between a sphere of radius $r_{s+l} = \alpha\sigma_c/2 + l$ and the cube. This volume can be estimated numerically using Monte Carlo (MC) integration.

For strands anchored *on the surface of the superball*, Ω_δ is calculated in a similar way, obtaining V_c^{tot}, that is the volume of a shell of width l around the superball (see Figure 3.2).

The volume of a superball with radius r and power n (see Equation 3.1) can be calculated either by MC integration or analytically as[39]:

$$V_c(r; n) = (2r)^3 \frac{(\Gamma(1 + 1/n))^3}{\Gamma(1 + 3/n)}, \tag{3.6}$$

where Γ is the Euler-Gamma function. From this, we can directly calculate the volume of the superball with radius $r_c = \sigma_c/2$ and power $n = 6$, $V_c(\sigma_c/2; n)$, which are the parameters used to capture the shape of the hematite cubes (see Methods). To obtain the volume of a constant shell of thickness l around such a superball, we then need the volume of a second superball with radius $r_{c+l} = \sigma_c/2+l$ controlled by the power n', $V_c(\sigma_c/2 + l; n')$ (also estimated using Eq. 3.6), from

which $V_c(\sigma_c/2; n)$ can be subtracted. The exponent n' is estimated numerically, yielding $n' = 5.55383$. We note that without using a superball with power n', we would get a wrong estimate of the shell volume, following a non-constant thickness around the first superball especially on the corners and the edges.

Therefore, the total volume V_c^{tot} of the shell around a superball of radius $\sigma_c/2$ and power n reads

$$\Omega_\delta = V_c^{tot} = V_c(\sigma_c/2 + l; n') - V_c(\sigma_c/2; n). \tag{3.7}$$

Once more, if the sphere is at interacting distance, we should also take into account the volume inaccessible to the strands. This corresponds to the volume of overlap between a sphere of radius $r_s = \alpha\sigma_c/2$ and the superball of power n' and radius $r_{c+l} = \sigma_c/2 + l$ (see Fig.3.2c). The value of Ω_δ in this case is given by

$$\Omega_\delta = V_c^{tot} - V_{over}(c + l, s), \tag{3.8}$$

where $V_{over}(c+l, s)$ is calculated via MC integration. Note that, $\Omega_{\gamma(\delta)}$ depends on the relative position of the sphere on the superball and on their reciprocal distance.

Finally, to estimate the configurational space available for the *two hybridized strands* $\Omega_{\gamma\delta}$, we follow a similar approach. We consider the sphere and superball with their corresponding shells of thickness l, and calculate their overlap region from which the inaccessible volumes due to steric effects has to be subtracted. This yields the volume that the two hybridized strands can explore, given by:

$$\Omega_{\gamma\delta} = V_{over}(c + l, s + l) - V_{over}(c, s + l) - V_{over}(c + l, s), \tag{3.9}$$

where the first term corresponds to the overlap of the two extended shapes, while the second and third terms represent the inaccessible volumes (see Figure 3.2). The green region in the figure corresponds to $\Omega_{\gamma\delta}$, while the red regions correspond to $V_{over}(c, s + l)$ and $V_{over}(c + l, s)$.

In all our calculations we fix the distance between the surface of the cube and the center of the sphere to $h = l + r_s$ (see also below) as schematically shown in Figure 3.2a. In Figure 3.2b, we present the numerical estimates for the available configurational spaces $\Omega_{\gamma(\delta)}$ and $\Omega_{\gamma\delta}$ depicted on the surface of the superball for an example size ratio $\alpha = 0.63$. As expected, $\Omega_{\gamma(\delta)}$ is constant all around the surface of the two colloids since it corresponds to the volume of a shell of thickness l around the sphere (cube). On the other hand, the configurational space available for hybridized strands varies depending on the reciprocal position of the sphere and cube, and it is highest at the center of the faces of the cube. This gives rise to the overall free-energy landscape, which is reported in Figure 3.7. For completeness, we summarize the schematics for the case in which $h = r_s$ in Figure 3.2c. In Figure 3.2d, we report the corresponding numerical estimates. We note that in this case the configurational space for the unbound strands $\Omega_{\gamma(\delta)}$ is different in different regions of the cube, with a minimum configurational entropy in the corners and edges of the cube. Nonetheless, despite a slightly different scale, the overall free-energy landscape $\beta\Delta G_{cnf}$ has similar features independently of the relative distance between sphere and cube h.

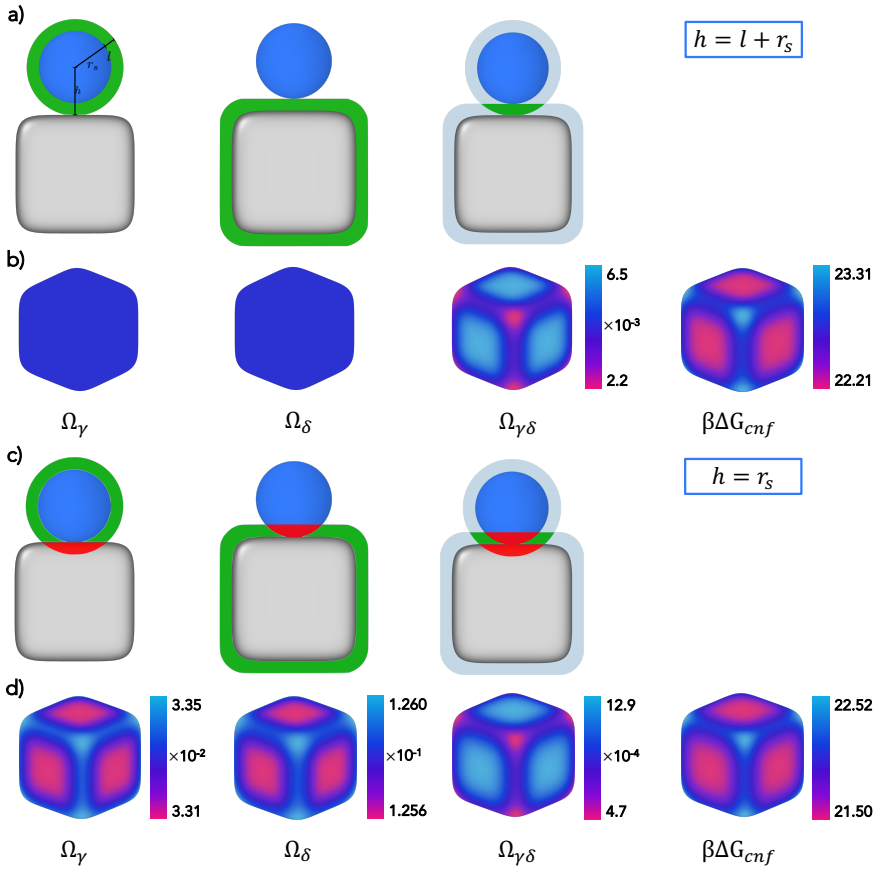

Figure 3.2: Schematics of the accessible configurational spaces for Ω_γ, Ω_δ and $\Omega_{\gamma\delta}$ for a distance between the center of the sphere and the surface of the cube.(a) $h = l + r_s$ and (c) $h = r_s$, respectively. The green regions indicate the accessible space for strands while the red regions are removed volumes because of the excluded volumes of the colloids. The computed accessible configurational spaces Ω_γ, Ω_δ and $\Omega_{\gamma\delta}$ displayed on the surface of the superball for $\alpha = 0.63$ are reported in (b) and (d) for two respective distances h. In (b), Ω_γ and Ω_δ are constant over the whole superball and equal to 0.0337 and 0.1263, respectively. $\Omega_{\gamma\delta}$ varies on the surface of the superball and takes values as indicated in the color bar. In (d), the configurational spaces differ depending on the relative sphere-cube position both in the unbound and bound states. Configurational spaces are given in units of σ_c^3. The results presented in the result section are for $h = l + r_s$.

Repulsive free energy

So far, we have only considered attractive interactions between a pair of strands. However, as the colloids get closer, the strands also give rise to an effective repul-

sion that adds to the steric repulsion experienced by the colloids. As detailed in reference,[25] this contribution can be calculated as

$$\beta F_{rep} = -\ln\left(\frac{V_c^{tot} - V_{over}(c+l,s)}{V_c^{tot}}\right). \tag{3.10}$$

Since we assume a constant surface distance h between the colloids, $\beta F_{rep} = 0$ as there is no overlap between a superball of radius $r_{c+l} = \sigma_c/2 + l$ and a spherical colloid of radius $\alpha\sigma_c/2$.

Total free energy

Once we have defined the individual contributions of two strands, we can calculate the *overall* free energy associated with linking a sphere and a superball in an arbitrary relative position Θ. Following the approximations made in reference,[34, 40] the attractive free energy of a system of two particles with complementary DNA strands γ and δ can be written as:

$$\beta F^{bond}(\Theta) = n_\gamma\left[\ln p_\gamma(\Theta) + \frac{1}{2} - \frac{p_\gamma(\Theta)}{2}\right] + N_s n_\delta\left[\ln p_\delta(\Theta) + \frac{1}{2} - \frac{p_\delta(\Theta)}{2}\right], \tag{3.11}$$

where n_γ and n_δ are the number of reactive DNA strands on a sphere and cube, respectively, and p_γ and p_δ are the bonding probabilities of the corresponding DNA types that are unhybridized.

The probabilities $p_{\gamma(\delta)}$ can be calculated using the following set of equations:

$$\begin{array}{rcl} p_\gamma + N_s n_\delta p_\gamma p_\delta \exp(-\beta\Delta G_{\gamma\delta}) & = & 1 \\ p_\delta + n_\gamma p_\gamma p_\delta \exp(-\beta\Delta G_{\gamma\delta}) & = & 1 \end{array} \tag{3.12}$$

where N_s is the number of spherical colloids. In the next section, we describe how we determined $n_{\gamma(\delta)}$, which is the other input parameter needed for the calculations.

3.2.4 Estimate of the Density of DNA Strands

Accurately estimating the number of strands that become embedded in the lipid bilayer solely based on the number of strands initially added to the system is challenging due to the uncertainty regarding the fraction of DNA that will successfully insert into the lipid layer. The experimentally employed nominal concentrations would correspond to one DNA linker per 50 nm^2 on the cubes and one inert DNA strand per 10 nm^2 on both particles if all strands are inserted. However, the hydrophobic cholesterol moeities of the linkers can also induce their assembly into small micellar-like clusters in solution. Thus, we expect there to be a balance between single DNA strands in solution, DNA strands in micelle-like clusters in solution, and inserted into the colloid supported lipid bilayer. Hence, the actual number of strands available for binding is lower than the number of strands added in the experiments. Moreover, the total number of reactive strands is affected by the presence of inert strands that are added as stabilizers.

Therefore, we estimate the number of strands on the surface of spheres and cube using the predictions of our microscopic model for the free-energy barrier experienced by the smallest spheres we investigate, which have a size ratio of $\alpha = 0.63$. Experiments have shown that for this size ratio, motion around the cube is not hindered. This means that the free energy barrier for moving from one face to the other passing through an edge cannot be higher than $O(10^1)\ k_BT$. If the barrier were higher, the configurational energy penalty for the strands would be too large, and the spheres would remain on the face of their initial adsorption.

To estimate the number of strands, we take several values of the total (reactive and inert) number of strands on the sphere, $n_\gamma^{tot} = n_\gamma + n_\gamma^{inert}$, and thus densities $\rho_\gamma^{tot} = n_\gamma^{tot}/A_s$ with A_s the surface area of the sphere, for the smallest size ratio α. We then calculate an approximate total number of strands on the cube, $n_\delta^{tot} = n_\delta + n_\delta^{inert}$, by fixing the surface density for both the spheres and the cube and using that the surface area of the cube in our case is $A_c = 4.9\sigma_c^2$. Here, we assume that, as a first approximation, there is no reason why the experimental procedure would give rise to an overall different density on the two colloid types. We then calculate the number of reactive and inert strands on each colloid, taking into account the density ratio between inert and reactive strands used in the experiments (see Methods). For spheres, this ratio is ≈ 330, while on the cube, the probability of having an inert strand is about five times higher than having a reactive one. We calculate βF_{bond} using Eq. 3.11 and perform Monte Carlo simulations based on the calculated free energy (see Methods). For each simulation, we calculate the autocorrelation function as defined in the result section and ensure that it decays within the simulation time. We present several examples in Figure 3.3 to show that for $\rho_\gamma = n_\gamma/A_s > 15$ (corresponding to a face-to-edge energy barrier higher than $\approx 11 k_BT$), motion on the surface of the cube is completely hindered, which would therefore contradict experimental evidence.

We choose a strand density of $\rho_\gamma = 11$ for the smallest investigated size ratio, which corresponds to a face-to-edge energy barrier of $\approx 7 k_BT$ and results in an autocorrelation function that decays within 10^4 MC steps (see Figure 3.3). This value is only slightly different from other lower densities, and a different choice of ρ_γ in this range does not significantly affect the results. We also note that this density estimate is reasonable as it allows us to calculate the typical DNA width d based on $\rho = 1/(ld)$[17], which gives a value of $d \approx 5$ nm, consistent with typical estimates for DNA width. Subsequently, we recompute $n_{\gamma(\delta)}$ for the higher size ratios while keeping the density of strands approximately fixed. The number of strands on the cube n_δ remains constant, as the cubes are the same for all size ratios. We have further verified that in all cases, the number of reactive strands present on the cube is sufficient for the reactive strands to form DNA patches on all spheres. Table 3.2 presents the parameters used for calculating the free energy for all the investigated size ratios.

Figure 3.4 illustrates the impact of varying $\rho_{\gamma(\delta)}$ on the change in free energy that the sphere experiences as it moves from the center of a face to an edge, i.e., $\beta\Delta F_{edge}$, for all size ratios. The left panel of Figure 3.4 shows the effect of varying the density of strands ρ_γ on a sphere, while keeping the density of reactive strands on the cube fixed so that $n_\delta = 3000$. The right panel, on the other hand, shows the opposite scenario, where n_γ is fixed to the values reported in Table 3.2. We

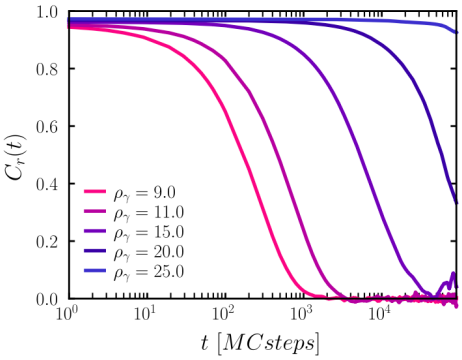

Figure 3.3: Position autocorrelation function $C_r(t)$ as a function of simulation time reported in MC steps for different strand densities in the sphere ρ_γ as indicated in the legend.

	Sphere			Cube		
α	n_γ	n_γ^{inert}	n_γ^{tot}	n_δ	n_δ^{inert}	n_δ^{tot}
0.63	14	4676	4690	3000	15000	18000
0.93	30	10020	10050	3000	15000	18000
1.20	50	16700	16750	3000	15000	18000
1.49	77	25718	25795	3000	15000	18000
1.98	136	45424	45560	3000	15000	18000
3.20	352	120908	121270	3000	15000	18000
4.44	682	227788	228470	3000	15000	18000

	Sphere			Cube		
	ρ_γ	ρ_γ^{inert}	ρ_γ^{tot}	ρ_δ	ρ_δ^{inert}	ρ_δ^{tot}
	≈ 11	≈ 3705	≈ 3716	≈ 613	≈ 3061	≈ 3674

Table 3.2: Parameters employed for the calculation of the free energy βF_{bond} for the size ratios α investigated: n_γ number of strands in the sphere, n_γ^{inert} number of inert strands in the sphere, n_γ^{tot} total number of strands in the sphere, n_δ number of strands in the cube, n_δ^{inert} number of inert strands in the cube, n_δ^{tot} total number of strands in the cube, and the corresponding strand densities.

note that choosing a larger value of n_γ would cause the free energy barrier to increase excessively, making it difficult to observe motion of the spheres. On the contrary, increasing the number of strands on the cube would not result in any differences in the free energy barrier. This is consistent with our expectations, given that the number of strands on the spheres constitutes the upper limit for binding. Furthermore, this also supports the assumption of treating each sphere independently in the calculation of free energy, assuming $N_s = 1$. This is because the number of strands on the cube is sufficient to allow for bond formation for all the spheres at all size ratios.

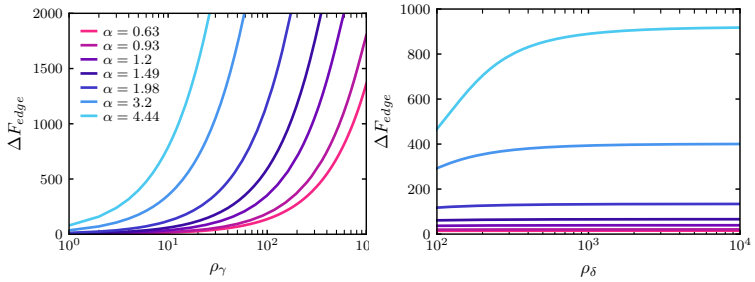

Figure 3.4: Free-energy difference $\beta\Delta F_{edge}$ between the center of a facet of the cube and a point on an edge (left) for varying density of strands on the sphere ρ_γ at fixed number of strands on the cube $n_\delta = 3000$ and (right) for varying density of the strands on the cube ρ_δ at a fixed number of strands on the spherical colloid for each size ratio (see Table 3.2).

Monte Carlo simulations

To study the mobility of the spheres on the surface of the superball, we perform Monte Carlo simulations based on the free energy βF^{bond}. The free energy βF^{bond} is calculated by setting the number of spheres to $N_s = 1$, regardless of the number of bonded spheres for each size ratio. We note that varying N_s and taking $\beta F_{pair} = \beta F^{bond}/N_s$ as the energy experienced by a sphere on the surface of the superball would result in a different estimate by at most $\approx 4\%$ for the highest size ratio. Therefore, for simplicity, we take $N_s = 1$ as the pair interaction energy for all size ratios, assuming the binding behavior of each colloid to be independent. This assumption is further supported by Figure 3.4, which shows that above a certain number of strands n_δ embedded on the cubic colloid, the difference in free energy experienced by a sphere at different positions on the cube does not vary. In our system, n_δ available for binding is sufficiently high to not observe any change in the free-energy landscape when more spherical particles are bonded.

We initialize the system by randomly placing on grid points of the cube the number of spheres as observed in the experiments for a specific size ratio α. MC moves are then attempted to one of the nearest-neighbor points on the surface grid of the cube using the Metropolis algorithm, which is appropriately corrected for the number of neighbors of each surface point. We first equilibrate the system for 10^5 MC steps before recording trajectories for at least 10^7 MC steps. For each size ratio, we run at least 20 independent simulation runs. We also consider the effects of experimental gravitational height, where the assembly and motion of spheres are restricted in space depending on the size of the bonded spheres. For size ratios $\alpha \geq 1.49$, the motion is confined to quasi-two-dimensional conditions, which excludes the upper and lower faces of the cube. No such restriction is imposed for smaller α.

3.3 Results and Discussion

3.3.1 Assembly of Colloidal Molecules with Controlled Flexibility and Directionality

We create colloidal molecules with controlled flexibility and directionality by assembling spherical silica particles onto the surface of cubic colloids, see Figure 3.5. We used solid silica spheres in combination with rounded cubic particles (whose shape can be described as superballs[29]) made of hematite [27] and coated with a thin silica layer by a Stöber procedure.[28]

To achieve flexible bonds, we exploited a method previously developed by some of us with modifications:[13, 14, 16] the particles were functionalized with a lipid bilayer that contained dsDNA strands with and without a 11 bp single stranded end that act as linkers and steric stabilizers, respectively, see Figure 3.5a. Since colloids coated with mobile linker DNA are able to bind more quickly to surfaces with higher receptor density,[36, 41] we here employed 300 linker DNA strands/μm^2 on the spherical and 20000 linker DNA strands/μm^2 on the cubic surfaces that act as complementary linkers. In addition, we added inert DNA strands at a nominal concentration of 1×10^5 linkers/μm^2 to both particles. After mixing, the complementary functionalized cubes and spheres bind to each other by accumulating DNA linkers in the area of closest contact. In this way, a so-called DNA *patch area* is formed, as shown in Figure 3.5f. We do not expect all added DNA strands to become included into the lipid bilayer. However, we use these nominal concentrations because they were empirically found to balance mobility with high binding probability. The low concentration of DNA strands on the spheres limits the number of bound DNA linkers and in this way ensures mobility of the colloids after binding.[14] The high linker concentration on the cubes provides fast binding of the spheres, even for the consecutive adsorption of spheres, because linker accumulation in the bond area does not lead to significant depletion of linkers on the cube surface.[36, 42] In the Methods section, we report further experimental details and the DNA sequences employed.

In a typical experiment, we mixed the DNA-functionalized cubes with an excess number of spheres (cube-to-sphere number ratio 1:20) and transferred them to a customized sample holder, where polyacrylamide(PAA)-coated coverslips were used as a substrate and cover on the top. During self-assembly, the excess number of spheres and the higher concentration of linker DNA on the cubes leads to faster binding of spheres onto the cubic particles and the formation of finite-size clusters, the flexible colloidal molecules, see Figure 3.5b, c, and g. After 12 hrs, the sample holder contained clusters and unbound spheres at the bottom. To remove excess spheres, we utilized the magnetic property of the hematite cube and isolated the flexible colloidal molecules by a handheld magnet. We did so by dispersing, separating and redispersing the colloidal molecules in buffer twice (200mM NaCl, 10mM HEPES, pH 7.4) (Figure 3.5d), which lead to a significantly increased purity and concentration of flexible colloidal molecules, see Figure 3.5h.

The cubic shape of the central particle allows for precise control over the maximum and most probable number of bound spheres by acting as a guiding template. The resulting colloidal molecules are of type AB_N, where A indicates

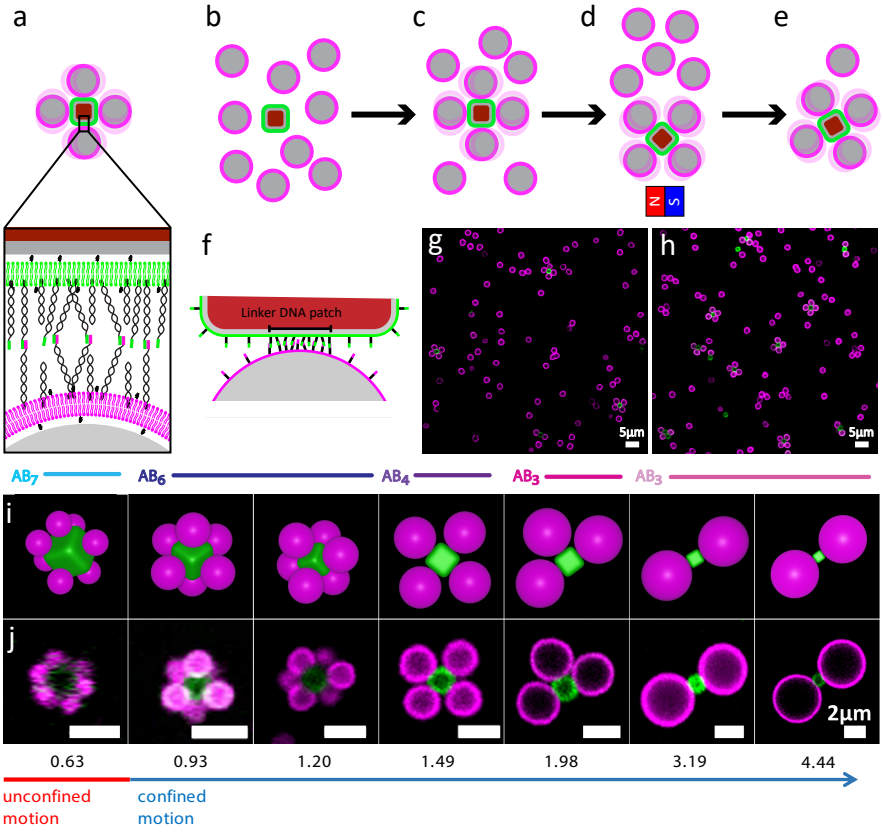

Figure 3.5: Self-assembly of colloidal molecules with controlled flexibility and bond directionality. (a) Schematic of a flexible colloidal molecule consisting of spheres (magenta) assembled onto a cube (green) and close-up view showing their functionalization with a lipid bilayer and surface-mobile DNA strands, where colored ends indicate different linker sequences. (b) The functionalized cubes and spheres are combined at a ratio of 1:20, which (c) enables rapid saturation of the cubic particles and ensures the formation of colloidal molecules. (d) The permanent magnetic dipole moment of the cubic particles is used to isolate the colloidal molecules by placing a magnet near the sample and removing the excess spheres, leading to (e) isolated flexible colloidal molecules. (f) Schematic indicating the patch formed between DNA linkers. (g) and (h) shows representative confocal microscopy images of assembled flexible colloidal molecules prior to and following isolation. (i) Schematics of the AB_N assembled clusters and (j) representative confocal microscopy images of the most likely type of experimentally obtained colloidal molecules for varying sphere-to-cube size ratios $\alpha = 0.63, 0.93, 1.20, 1.49, 1.98, 3.19,$ and 4.44 (from left to right). For $\alpha = 0.63$, the spheres move indistinctly on different faces of the rounded cube, while an increasingly confined motion on single faces occurs for higher α.

the cube, B the spheres and N the coordination number. We employed different size ratios of the sphere diameter σ_s to cube edge length σ_c, $\alpha = \sigma_s/\sigma_c$= 0.63, 0.93, 1.20, 1.49, 1.98, 3.19, and 4.44. The size of the cubic particles cannot be varied largely, and hence different size ratios are achieved by varying the size of the spheres. In this way, we find different values of the number of spheres attached to the cube, with more than six spheres attached for the lowest size ratios and with at maximum one sphere per facet for $\alpha \geq 1.20$. Schematic representations and confocal microscopy images of the resulting flexible colloidal molecules are shown in Figure 3.5i and j respectively, for the studied size ratios. We note that magnetic separation works well for size ratios from 0.63 to 1.49, but for larger size ratios from 1.98 to 4.44, we found that the increased size of the sphere caused the bond between the sphere and cube to break easily during separation.

The most probable coordination number of the colloidal molecules is the result of two factors. First, it is based on packing considerations, according to which each bounded sphere limits the available space for others to bind depending on its excluded volume.[18, 43] This effect has been extensively explored to increase the yield and sharpen the cluster size distribution for flexible colloidal molecules made of spheres only,[18] for electrostatically assembled rigid colloidal molecules made from spheres and cubes,[44] and for polyhedra in confinement.[45, 46] Here, no external confinement is present which could affect the guiding effect of the cubic shape on the position of the spherical particles. Also, the anisotropic cubic surface could lead to a non-conformal distribution of the linkers that could cause an effectively different shape, as was previously shown for nanoparticles.[47, 48] However, for the colloidal particles employed here an eventual non-uniform distribution of much smaller linkers will not significantly affect their shape. For the electrostatic assembly of cubes and spheres, colloidal molecules with coordination number 6, AB_6, were found for sphere-to-cube size ratio $\alpha < 2$, while AB_4 and AB_2 type colloidal molecules were predominantly observed at around $\alpha \approx 3$ and for $\alpha > 3$, respectively. For the present case, the cubic particle at the center provides a similar template that guides the position of the spheres. Indeed, for $\alpha \geq 1.20$ we find approximately the same coordination numbers, as evidenced by the most likely cluster shown in Figure 3.5i and j. Differently from rigid colloidal molecules, we find that longer times are typically required for establishing the flexible bonds between DNA linkers, and hence we allowed assembly to continue for 12 hours instead of the 15 minutes that are typically required for rigid colloidal molecules.[44] We also found that employing a high number of DNA linkers on the cubic particles together with low DNA concentrations on the spheres increases the yield of colloidal molecules with maximum valence. The reason is that this combination retains mobility by limiting the number of bound linkers through the low concentration of linkers on the spheres. At the same time, it enables to maximize the number of bound particles on the cube because it avoids depletion of linkers on the cubes upon binding of the spheres. The experimental cluster size distribution for the analyzed size ratios is reported in Figure 3.6.

The coordination number of the colloidal molecules is also influenced by the gravitational height which effectively confines larger spheres to quasi-2D, see Table 3.3. For low α = 0.63, 0.93 and 1.20, we can employ small spheres which diffuse in three dimensions. Therefore, assembly occurs mainly in three-dimensional con-

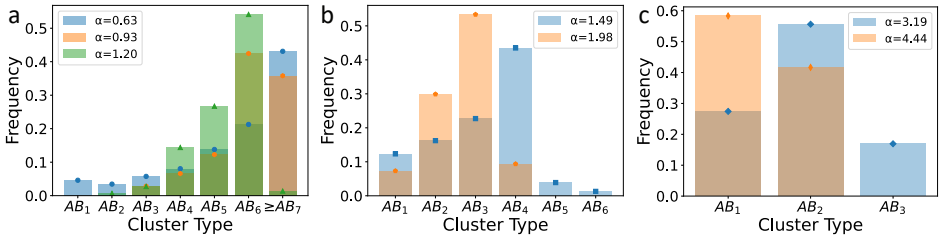

Figure 3.6: Cluster size distribution for varying sphere-to-cube size ratios a) α=0.63, 0.93 and 1.20. b) α=1.49 and 1.98, and c) α=3.19 and 4.44.

Table 3.3: Gravitational height of the silica particles used in the study.

Diameter of Sphere (μm)	Gravitational Height (nm)
0.66±0.01	2.8×10^3
0.97±0.05	8.8×10^2
1.25±0.05	4.1×10^2
1.55±0.05	2.2×10^2
2.06±0.05	92
3.32±0.05	22
4.62±0.05	8.1

ditions and yields predominantly AB_6-type colloidal molecules. For higher size ratios which require larger spheres we mainly retrieve two-dimensional constructs, as the spheres quickly settle to the bottom of the container and assembly occurs under quasi-2D conditions. Hence, as at most only one sphere binds per facet, AB_4 and AB_3 colloidal molecules are obtained at $\alpha = 1.49$ and 1.98, respectively. Further increasing the size ratio above $\alpha = 3.19$ forces the spheres to bind to opposite sides of the cube due to steric constraints, forming mostly AB_2 colloidal molecules.

By utilizing surface-mobile DNA strands, the spheres of the fabricated colloidal molecules are able to diffuse on the faces of the cube. In particular, we observed that for the smallest size ratio, the spheres can move between different facets, whereas in the other cases, the motion is limited to the same facet of adsorption. In the following sections, we will first theoretically explore the reasons behind this behavior, and then conduct a comprehensive analysis of the conformational flexibility of the assembled colloidal molecules.

3.3.2 Origin of Constrained and Unconstrained Motion of Flexible Colloidal Molecules

The cubic shape, in combination with the multivalent bonds, plays a crucial role in enabling the spatially constrained motion of the adhered spheres and the conformational flexibility of the colloidal molecules. As previously mentioned, the bond

between the spheres and cubes is composed of numerous bound DNA linkers within a patch area (see Figure 3.5f). The size and shape of this area are determined by two factors: i) the distance at which two DNA linkers can still bind and ii) the shape, dimension, and relative position of the two bound particles. The motion of the spheres on the surface of the cube requires rearrangement and shrinking of the DNA patch at the edges and corners in comparison to the face.[14] As a result, all the strands comprising the patch will change from their original positions in the lipid bilayer. In case the energy required for this rearrangement exceeds the thermal energy, crossing around a corner or edge of the cube may occur less frequently.

To identify the nature of the constrained and unconstrained motion for different sphere-to-cube size ratios, we calculate the free energy experienced by the spheres on the surface of the cube when bonding between DNA strands occurs. To this end, we adapted a microscopic model that retains all the essential features of the physics of DNA-mediated interactions, including their mobility on the surface to the geometry of our system,[25, 40] to the geometry of our system. This model was used to describe various self-assembly processes of colloids with a fixed strand position on their surfaces,[40, 49–51] and then extended to account for mobile linkers.[17, 25, 35, 36, 52–56] In the initial step, we compute the free energy $\beta\Delta G_{\gamma\delta}$ of a bond between two DNA strands γ and δ, given by

$$\beta\Delta G_{\gamma\delta} = \beta\Delta G_0 + \beta\Delta G_{cnf}, \tag{3.13}$$

where $\beta = 1/k_BT$ with k_B the Boltzmann constant and T the temperature. The first term, ΔG_0, refers to the DNA hybridization free energy, while the second term, ΔG_{cnf}, denotes the configurational cost linked to bond formation. ΔG_0 is dependent of the DNA sequence employed in the strands and varies with temperature. We calculate its value using the nearest-neighbor SantaLucia rules[32] with an inert tail correction[33]. Once two strands are hybridized, their available configurational space is reduced as compared to two unhybridized strands,[34, 50, 57] and this is captured by:[25]

$$\beta\Delta G_{cnf} = -\ln\left(\frac{1}{\rho_0}\frac{\Omega_{\gamma\delta}}{\Omega_\gamma\Omega_\delta}\right), \tag{3.14}$$

where ρ_0 is the reference concentration, $\Omega_{\gamma(\delta)}$ is the configurational space available for the strand $\gamma(\delta)$ when unhybridized on the sphere (cube), and $\Omega_{\gamma\delta}$ is the configurational space for a pair of hybridized strands. The configurational space of unbound linkers consists of the volume of a shell around the surface to which the DNA linkers are attached with a width equal to the length of the linker. l[25] Instead, hybridized strands will be able to explore only the region where the configurational spaces of the sphere and cube overlap, see schematics in Figure 3.7a and Figure 3.2.

We use Monte Carlo integration to estimate the available configurational spaces for different positions of the sphere on top of the cube. To simplify the theoretical treatment, we set the normal distance between the center of the sphere and the surface of the cube to $h = l + \sigma_s/2 = l + \alpha\sigma_c/2$. This allows us to neglect the repulsive contributions arising from inert and reactive DNA strands on the lipid

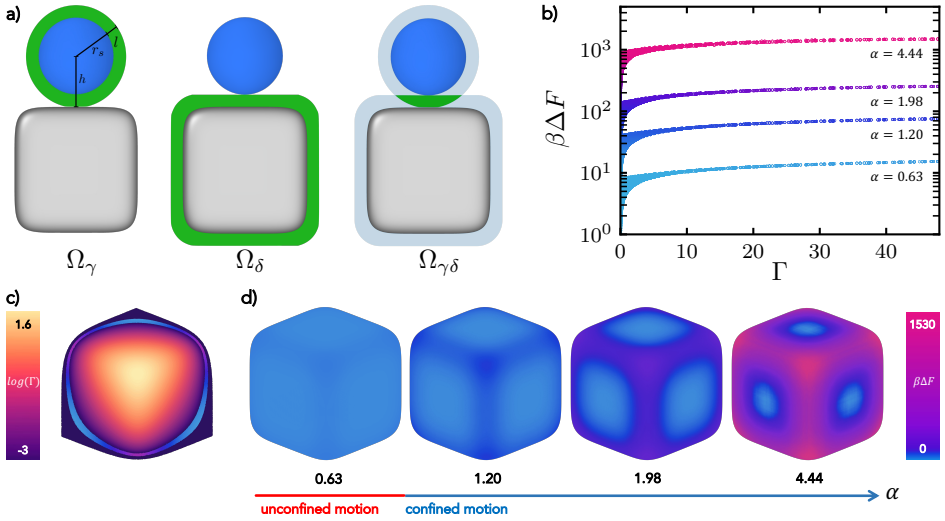

Figure 3.7: Origin of constrained and unconstrained motion. (a) Schematics showing the configurational space Ω_γ, Ω_δ and $\Omega_{\gamma\delta}$ available for mobile strands when these are located on the spherical colloids, on the cube, and for hybridized strands, respectively. Sphere and cube are located at a distance $h = \sigma_s/2 + l = r_s + l$, with l the length of a DNA linker and r_s the radius of the sphere. The green color indicates the available configurational space for the strands in each case, while light blue in $\Omega_{\gamma\delta}$ represents the shell of thickness l where the strands are able to move in when unhybridized. (b) Free energy barrier $\beta\Delta F$ as a function of the Gaussian curvature Γ of the cube which is parametrized as a superball for the four different size ratios analyzed, namely $\alpha = 0.63, 1.20, 1.98$ and 4.44. (c) Gaussian curvature depicted on an octant of the superball. For a band of the octant with (similar) low curvature, we also report the corresponding free energy. For the other octants, the free-energy landscape is the same due to the symmetry of the superball. The color scale for the free energy in the band is the same as in (d). (d) Free energy barrier $\beta\Delta F$ reported on the surface of the superballs for the four different size ratios analyzed in (b).

bilayers.

We then extend the calculation of the free energy to multiple mobile strands,[25] obtaining βF^{bond}, for which an estimate of the overall number of strands is needed. Since it is difficult to quantify the fraction of reactive and inert strands that are embedded in the lipid bilayer from experiments, we rely on the predictions of our microscopic model. In particular, we choose the number of strands as the threshold value above which the motion of the spheres for the smallest size ratio studied would be constrained. For higher size ratios, we then use the same strand density as the one used for the smallest size ratio.

In this way, we can calculate $\beta\Delta F = \beta F^{bond}_{face} - \beta F^{bond}$ as the difference in free energy experienced by a sphere when it moves from the center of a cube face, where the configurational entropy is maximised (see Figure 3.2), to another position on

its surface. To achieve this, we construct a fine discrete grid using the equation for a superball to describe the cubes surface[29] (see Methods), allowing us to obtain βF^{bond} for each point. We plot this quantity as a function of the Gaussian curvature Γ of the rounded cubes for four different size ratios α in Figure 3.7b. In Figure 3.7c, we show Γ for an octant of a cube/superball with $\alpha = 4.44$.[30, 31] The free energy $\beta\Delta F$ is also depicted directly on the surfaces of the superballs in Figure 3.7d. We observe that the free-energy barrier for moving across the edges increases as the diameter of the sphere increases from $\alpha = 0.63$ to $\alpha = 4.44$, consistent with our expectations. Specifically, we find that $\beta\Delta F$ increases from a few k_BT for the smallest size ratio to hundreds of k_BT for the highest size ratio. Since we assume in our calculation that ΔG^0 is constant for all DNA strands, the observed increase in $\beta\Delta F$ with increasing size ratio α can be attributed to the reduced configurational entropy of the bound strands located at the edges, compared to those on the faces of the superball (see also Figure 3.2). Consequently, the mobility of the attached sphere is impeded and the probability of crossing from one face to another decreases for larger spheres.

Additionally, we observe that for each size ratio the largest value of the free-energy barrier is located at the highest curvature, which corresponds to the value measured at the corners of the rounded cube. This finding confirms that the probability for spheres to be primarily located at the center of the cube faces, where $\Omega_{\gamma\delta}$ is the highest, is enhanced. We also observe that in all cases, the system exhibits an increasingly wider range of free energies as Γ approaches zero. This can be explained by examining Figure 3.7c, which shows both Γ and $\beta\Delta F$ for a narrow band of the superball where the curvature has approximately the same (low) values. Within this band, we notice that as we move from one face of the cube to the other, we cross an edge region where the free energy varies significantly. This counter-intuitive phenomenon is attributed to the differences in the configurational space that bound strands in the patch located in these two regions would experience, resulting in different free energies for sites with similar curvature. In contrast, if we had a surface with a constant curvature that was infinitely large, the free energy would remain constant across the entire surface.

3.3.3 Impact of Size Ratio on the Flexibility of the Colloidal Molecules

Using a microscopic model for the DNA interactions between the colloids, we found that the size of the spheres has a significant effect on the free energy of the system. By changing the size ratio between the spheres and the cube and thus altering the features of the DNA patch, we not only have access to different coordination numbers but we also expect to have control over the conformational flexibility of colloidal molecules by adjusting the energetic barrier between different conformations. Eventually, this control will enable us to observe a transition from unconstrained motion, where spheres are able to move across various facets, to motion constrained to a single facet of the rounded cube.

In the experiments, we thus first focus on two size ratios, namely $\alpha = 0.63$ and 0.93, and on a colloidal molecule with four spheres attached. We intentionally introduced damage to the PAA coating to (partially) immobilize the flexible

colloidal molecules by adhesion to the glass slide and subsequently selected one with an immobilized cube and mobile spherical particles (see Methods). In this way, it is possible to easily track the motion of the spheres on the central cubic particle and the results for the two different size ratios are not affected by excluded volume effects. Figure 3.8a and b report the experimental time-lapse microscope images and the trajectories of the spheres over time for both size ratios α. For the smallest size ratio $\alpha = 0.63$, we observed that the spheres move smoothly between the different faces of the cube, implying that they were able to cross its edges. Correspondingly, the trajectories of the attached spheres show how the spheres are able to diffuse on the surface of the cube giving rise to an unconstrained motion. This picture drastically changes when studying $\alpha = 0.93$. In this case, the motion is restricted to the facets of the cube, with the spheres always exploring the same facet where they initially bound to, as evident from the particle trajectory shown in the rightmost panel of Figure 3.8b. We note that the large spread in the linker distribution within the sample leads to some colloidal molecules at size ratio $\alpha = 0.93$ to still show unconfined motion, while the majority displays confined motion of the spheres. Thus, the spread in the linker distribution causes a gradual transition from unconfined to confined motion with increasing size ratio.

To gain further insights, we study the motion of spheres on the rounded cube using Monte Carlo (MC) simulations. For this purpose, we randomly place the same number of spheres as in the experiments on the surface of the cube and use the free-energy calculations presented earlier as a criterion for attempting an MC move on the surface of the cube, using the same density of inert and reactive DNA strands for both size ratios. More information can be found in the Methods section. Our simulations show that we indeed recover a similar behavior as in experiments. Simulation snapshots and the corresponding regions of the cube explored by the four spheres are shown in Figure 3.8c and d for $\alpha = 0.63$ and 0.93, respectively. Such regions are made up by the corresponding contact points of the spheres onto the superball and are colored differently for different spheres. In agreement with experiments, we observe that the increase in size ratio from $\alpha = 0.63$ to $\alpha = 0.93$ corresponds to a transition from unconstrained to constrained motion. Indeed, we observe that small spheres with $\alpha = 0.63$ change multiple times between facets, implying that their movement is free on the surface of the cube and across faces (see Figure 3.8c).

This behavior is also reflected in the decay of the position autocorrelation function, defined as $C_r(t) = \sum_{i=1}^{N}(1/N)(\mathbf{r}_i(0) \cdot \mathbf{r}_i(t))/\mathbf{r}_i(0)^2$, where the sum runs over all bounded particles $N = 4$, $\mathbf{r}_i(0)$ and $\mathbf{r}_i(t)$ are the initial position and the position at time t, respectively, of the ith sphere. Note that the positions are taken as the corresponding position of the sphere on the surface of the cube. As shown in Figure 3.9 for $\alpha = 0.63$, $C_r(t)$ starts already decaying after 10^4 MC steps, implying that particles indeed diffuse freely on the surface of a cube. On the contrary, for $\alpha = 0.93$, we confirm the confined movement on the initial faces of adsorption, with $C_r(t)$ not decaying even at long times.

The study of the dynamics of the spheres on the surface of the rounded cube can also be extended to colloidal molecules with a sphere-to-cube size ratio that exceeds 0.93. In simulations, we assess the most frequently experimentally assembled cluster for each size ratio α and we constrain the motion of the spheres

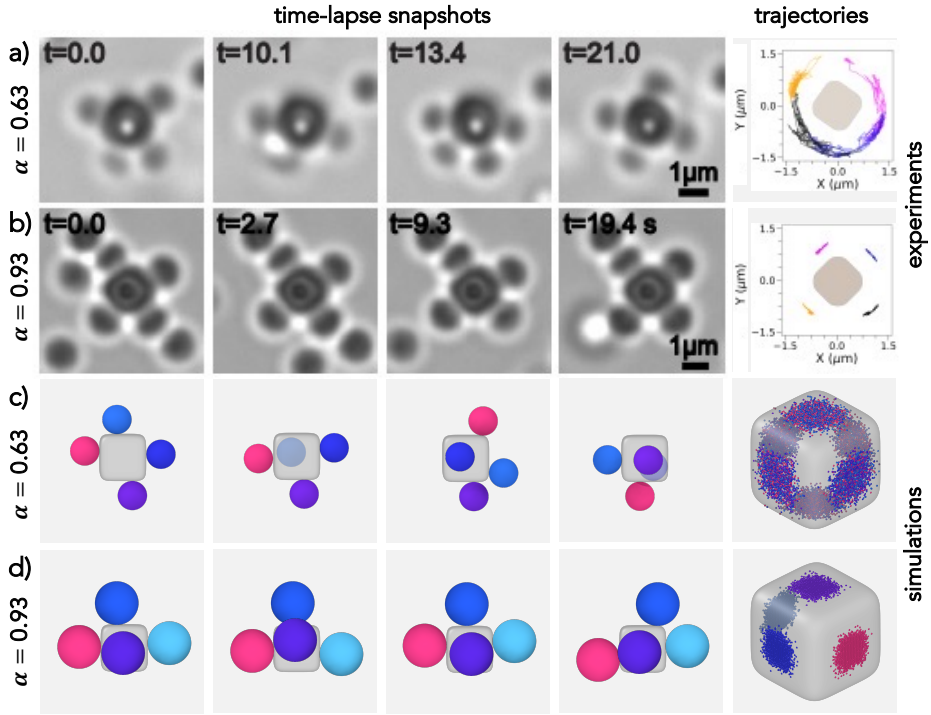

Figure 3.8: Transition from unconstrained to constrained motion. Time-lapse snapshots of microscope images showing the sphere motion on the cube for (a) $\alpha = 0.63$ (unconstrained motion) and (b) $\alpha = 0.93$ (constrained motion). The rightmost panel reports the trajectories of the spheres on the surface of the cube. (c,d) Three-dimensional time-lapse simulation snapshots and trajectories for the same size ratios as in (a) and (b), respectively. For each α, the snapshots always have a fixed orientation and particles with the same identifier are colored alike. The rounded cube always has the same dimension in the two cases. As in (a,b), the rightmost panels reports the trajectories of the sphere on the surface of the cube.

in the z-direction to mimic the effect of the experimentally observed quasi two-dimensional confinement. Configurations adopted by such colloidal molecules and particles trajectories are shown in Figure 3.10a and b, respectively. Consistently with the previous observation for $\alpha = 0.93$, we notice that the sphere motion is always restricted to the same facet. Nonetheless, these colloidal molecules with limited mobility of the spheres still retain a discrete amount of flexibility, which in these cases thus refer to the ability of the spheres to explore the face they are bound to. While all colloidal molecules indeed possess some flexibility, the range of motion of the attached spheres reduces with increasing size ratio. This can be observed by looking at the regions explored by the spheres reported in Figure 3.10b, where the scattering of the sphere's contact points is progressively reduced for higher α. This phenomenon is due to the increased patch size of the

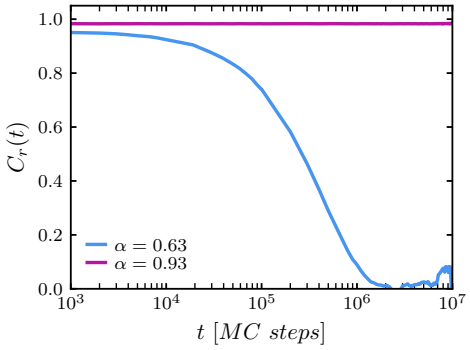

Figure 3.9: Position autocorrelation function for $\alpha = 0.63$ and 0.93 as a function of the simulations time reported as MC steps.

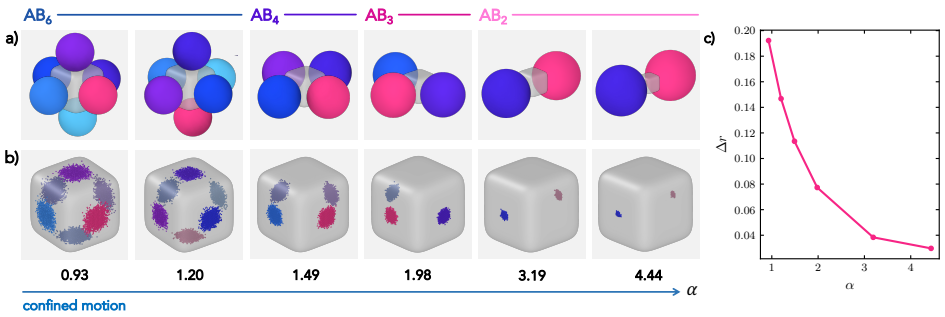

Figure 3.10: Confined motion. (a) Simulation snapshots showing an exemplary configuration of the spheres with respect to the central cube and (b) trajectories of the points of contact of the bound spheres for varying sphere-to-cube size ratios $\alpha = 0.93, 1.20, 1.49, 1.98, 3.19$, and 4.44 (from left to right). For better visualization, the points of contact are reported every fifty Monte Carlo (MC) steps. Different colors are employed to distinguish different spheres. (c) Mean displacement of the spheres on the surface of the superball Δr as a function of the size ratio α.

bound DNA linkers with respect to the cube size, which implies that the spatial limitation by the cube facet is already experienced at smaller displacements from the center of the facet. In fact, more linkers will retain a reduced configurational entropy. Thus, with increasing α, a further decrease of the flexibility is observed. Besides, steric constraints imposed by the presence of spheres on adjacent facets of the cubes can further reduce the range of motion at higher size ratios for the same coordination number N. The colloidal molecules thus obtained not only differ in coordination number but also in conformational flexibility. We quantify the confinement in the motion by calculating in simulations the mean displacement of the spheres as $\Delta r = \sqrt{\lim_{t\to\infty} \sum_{i=1}^{N} |\mathbf{r}_i(t) - \mathbf{r}_i(0)|^2 / N}$, where we assumed the surface area in which the sphere motion occurs to be flat. We report the latter as

a function of the size ratio α in Figure 3.10c. The progressive decrease in the size of the region explored by the spheres confirms the presence of constrained motion which is progressively restricted towards $\alpha = 4.44$ by about five times.

3.3.4 Temperature-Induced Reversible Transition of Flexible Colloidal Molecules from Constrained to Unconstrained Motion

The free-energy difference experienced by the spheres hinges on the DNA-based bonding patch. While the maximum configurational entropy difference between the facet and edge is determined by geometry alone, the enthalpic and entropic contributions for the formation of the DNA patch depends on the number of bound DNA linkers. Therefore, a change in the number of bound DNA linkers in the patch tunes the free-energy landscape, providing an additional mean of controlling the conformational flexibility and eventually the confinement of the motion of the spheres. We experimentally realize this by exploiting the temperature dependent binding probability of the DNA linkers, which is controlled by the DNA hybridization free energy ΔG^0. Increasing the temperature close to the melting temperature reduces the number of bound linkers and hence increases the probability of a sphere to cross to other facets.

We demonstrate the temperature dependent conformational flexibility with a flexible colloidal molecule with three bound spheres for $\alpha = 0.93$. Again, we immobilize the colloidal molecules to be able to track the particle motion (see Methods). At room temperature, the spheres are mobile but confined to their respective faces as visible from the snapshots and trajectories of the spheres in Figure 3.11a. When the sample is heated to 35.9 °C, the same flexible colloidal molecule now exhibits full conformational flexibility, and the spheres bound to cubes are able to move freely from one face of the cube to another. After the sample has been brought down to room temperature, the motion of the spheres once again is confined to the individual faces of the cube as seen from Figure 3.11c. The reversible change in conformational flexibility of this flexible colloidal molecule persists upon repeatedly heating and cooling the sample. We note that one sphere remains confined to its side for the length of the video at high temperature. This may be due to the sphere also being partially immobilized. Alternatively, it might stem from it having a higher DNA density, as the density of DNA linkers on a given sphere can vary by an order of magnitude[14, 36] and hence even at higher temperature too many bonds may persist causing its motion to be constrained. This effect is similar to the one discussed earlier, when we noted a gradual transition from unconfined to confined motion upon changing the size ratio. During cooling cycle at lower temperature, the sphere achieved full mobility and became subsequently confined at the top of the cube. Therefore, only two traces are visible in Figure 3.11c.

We complement our experimental observations by investigating the effect of temperature on the conformational flexibility of the colloidal molecules via simulations (see Methods). We keep the value for the number of strands that was determined earlier for $\alpha = 0.93$, and compute the DNA hybridization free energy ΔG^0 at two higher temperatures, namely $T = 36°C$ and $40°C$. Based on these updated free energies, we carry out new MC simulations. We do not consider

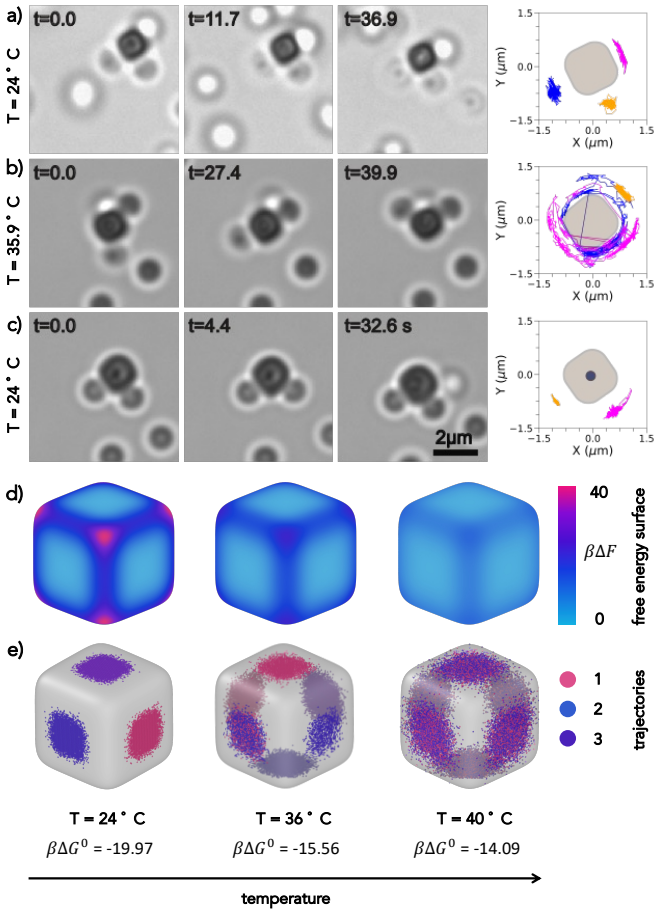

Figure 3.11: Temperature-control over conformational flexibility. (a-c) Bright field microscopy snapshots and corresponding trajectories of a flexible colloidal molecule with $\alpha = 0.93$ showing a reversible transition of constrained to unconstrained conformational flexibility. The cube has been immobilized on the substrate. (a) At room temperature $T = 24$ °C the diffusion of spheres is constrained to the respective faces of the cube. (b) Upon an increase in the temperature to $T = 35.9$ °C the same flexible colloidal molecule shows full conformational flexibility where spheres can cross the edges. (c) Cooling back to room temperature confines the spheres' motion again to the respective faces of the cube. (d) Free energy $\beta\Delta F$ reported on the surface of the superballs for $T = 24, 36, 40$°C, corresponding to three different values of the DNA hybridization free energy $\beta\Delta G^0$. (e) Trajectories of three spheres on the surface of the superball for the same temperatures as in (d). Different colors relate to the trajectories of different spheres.

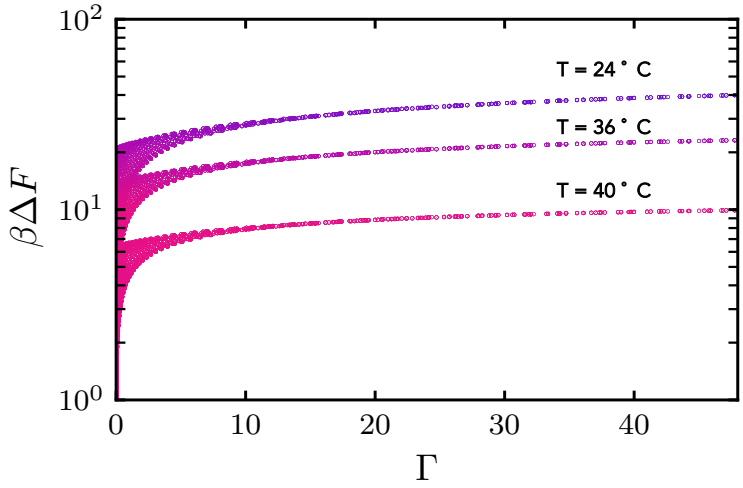

Figure 3.12: Free energy $\beta\Delta F$ as a function of the Gaussian curvature of the superball Γ for the three different temperatures analyzed, corresponding to $T = 24, 36, 40°\mathrm{C}$.

any effect in polydispersity of the strand number present in experiments since it could not be quantified precisely and because its effect is to make transitions from confined to unconfined less sharp upon change in size ratio or temperature.

For all cases, we report the free energy $\beta\Delta F$ and the particle trajectories on the surface of the cube in Figure 3.11d and e, respectively. In Figure 3.12, the free energies are reported as a function of the curvature of the superball. Our calculations show that, by increasing the temperature, the free-energy differences towards the edge progressively decreases. Therefore, consistently with experiments, the crossing probability for spheres increases with temperature at the size ratio analyzed. This is the reason why at the highest effective temperature studied the three particles can freely explore the entire surface of the cube, as shown in the right panel of Figure 3.11e. This phenomenon is similar to that observed earlier by decreasing the size ratio α between the sphere and the cube (see Figure 3.8 and3.10). However, in this case, the change in free-energy barrier is entirely determined by the DNA hybridization free energy ΔG^0, while the configurational entropy term remains constant.To summarize, the multivalent bonding patch together with the anisotropic shape of the cube provide therefore the necessary ingredients to confine the motion of the attached spheres and, by changing temperature, this constraint can be reversibly relieved and imposed on demand.

3.4 Conclusions

We assembled colloidal molecules with directional bonds and controlled conformational flexibility by employing cubic particles at their center. By varying the size ratio α between the spheres and cubes, we assembled flexible colloidal molecules

with different, well-controlled coordination number in high yields. We identified α, and thus the DNA patch size between the sphere and the cube, to be critical in restricting the diffusive motion of the sphere to the cube's face. At $\alpha = 0.63$, we find that spheres can easily diffuse across different faces of the cube, whereas their motion is constrained to a single face for $\alpha \geq 0.93$. Using a microscopical model, we find that the curvature variation of the cube leads to an effective free-energy landscape for the spheres' motion, with decreasing probability for crossing edges and corners with increasing size ratio. In addition, the motion on a given facet is increasingly confined due to the energetic costs associated with moving DNA linkers to the more highly curved edges. We quantified their confinement and ability to change face, and analyzed their equilibrium distributions according to the free energies. It will be interesting to compare our results with new experiments in the future that might be able to precisely quantify the number of strands incorporated into the lipid bilayer and measure their spatial arrangement on the colloid. Finally, we demonstrated that temperature can be used to reversibly switch between confined and unconfined motion of the spheres on the cubes' surface. The magnetic dipole moment of the hematite core of the cubic particles can be utilized to separate the flexible colloidal molecules for small size ratios.

The thus prepared, flexible colloidal molecules can serve as building blocks for the preparation of higher order structures with desired flexibility and can be used to study the influence of controlled conformational flexibility on their phase behavior,[58, 59] crystal formation, and reconfiguration, which is crucial in designing materials and their properties.[60–62] Our insights into how the geometry of a template shapes the free-energy landscape for the adhered spheres are relevant beyond an application to flexible colloidal molecules as they can be employed to design other flexible structures with controlled conformational flexibility. The ability to release and reimpose the confinement by a simple increase and decrease of temperature is a powerful strategy to rearrange and fixate the conformation of flexible colloidal structures at will, thereby opening a way to create *in situ* controllable functional devices and machines with multiple stable configurations.[63]

Acknowledgements

I acknowledge Fabrizio Camerin, Susana Marín-Aguilar, and Marjolein Dijkstra (Utrecht University) for their contribution to the computational part of this work. I thank Rachel Doherty for help in SEM imaging of particles and buying temperature set-up. I thank Melissa Rinaldin for helping with cubes synthesis. I thank Christine Linne, Samia Ouhajji, Julio Melio and Ali Azadbhakt for the fruitful discussions on DNA and colloidal synthesis.

3.5 Bibliography

[1] Alfons van Blaaderen. Chemistry: Colloidal molecules and beyond. *Science*, 301(5632):470–471, 2003.

[2] Wilson Poon. Colloids as big atoms. *Science*, 304(5672):830–831, 2004.

[3] Sharon C. Glotzer and Michael J. Solomon. Anisotropy of building blocks and their assembly into complex structures. *Nature Materials*, 6(8):557–562, 2007.

[4] Fan Li, David P Josephson, and Andreas Stein. Colloidal assembly: the road from particles to colloidal molecules and crystals. *Angewandte Chemie International Edition*, 50(2):360–388, 2011.

[5] Etienne Duguet, Anthony Désert, Adeline Perro, and Serge Ravaine. Design and elaboration of colloidal molecules: an overview. *Chemical Society Reviews*, 40(2):941–960, 2011.

[6] Étienne Ducrot, Mingxin He, Gi-Ra Yi, and David J Pine. Colloidal alloys with preassembled clusters and spheres. *Nature Materials*, 16(6):652–657, 2017.

[7] Mingxin He, Johnathon P Gales, Étienne Ducrot, Zhe Gong, Gi-Ra Yi, Stefano Sacanna, and David J Pine. Colloidal diamond. *Nature*, 585(7826):524–529, 2020.

[8] Susana Marín-Aguilar, Fabrizio Camerin, and Marjolein Dijkstra. Guiding the self-assembly of colloidal diamond. *The Journal of Chemical Physics*, 157(15):154503, 2022.

[9] P Mellado, A Iniesta, FG Diaz, and J García De La Torre. Diffusion coefficients of segmentally flexible macromolecules with two subunits: a study of broken rods. *Biopolymers: Original Research on Biomolecules*, 27(11):1771–1786, 1988.

[10] M. J. Betts and M. J. Sternberg. An analysis of conformational changes on protein-protein association: implications for predictive docking. *Protein Engineering*, 12(4):271–283, 1999.

[11] H Jane Dyson and Peter E Wright. Intrinsically unstructured proteins and their functions. *Nature Reviews Molecular Cell Biology*, 6(3):197–208, 2005.

[12] Pierre Illien, Tunrayo Adeleke-Larodo, and Ramin Golestanian. Diffusion of an enzyme: The role of fluctuation-induced hydrodynamic coupling. *EPL (Europhysics Letters)*, 119(4):40002, 2017.

[13] Stef AJ van der Meulen and Mirjam E Leunissen. Solid colloids with surface-mobile dna linkers. *Journal of the American Chemical Society*, 135(40):15129–15134, 2013.

[14] Indrani Chakraborty, Vera Meester, Casper van der Wel, and Daniela J Kraft. Colloidal joints with designed motion range and tunable joint flexibility. *Nanoscale*, 9(23):7814–7821, 2017.

[15] Angus McMullen, Miranda Holmes-Cerfon, Francesco Sciortino, Alexander Y Grosberg, and Jasna Brujic. Freely jointed polymers made of droplets. *Physical Review Letters*, 121(13):138002, 2018.

[16] Melissa Rinaldin, Ruben W Verweij, Indrani Chakraborty, and Daniela J Kraft. Colloid supported lipid bilayers for self-assembly. *Soft Matter*, 15(6):1345–1360, 2019.

[17] Angus McMullen, Sascha Hilgenfeldt, and Jasna Brujic. Dna self-organization controls valence in programmable colloid design. *Proceedings of the National Academy of Sciences*, 118(46):e2112604118, 2021.

[18] Indrani Chakraborty, Daniel JG Pearce, Ruben W Verweij, Sabine C Matysik, Luca Giomi, and Daniela J Kraft. Self-assembly dynamics of reconfigurable colloidal molecules. *ACS Nano*, 16(2):2471–2480, 2022.

[19] Ruben W Verweij, Pepijn G Moerman, Nathalie EG Ligthart, Loes PP Huijnen, Jan Groenewold, Willem K Kegel, Alfons van Blaaderen, and Daniela J Kraft. Flexibility-induced effects in the brownian motion of colloidal trimers. *Physical Review Research*, 2(3):033136, 2020.

[20] Ruben W Verweij, Pepijn G Moerman, Loes PP Huijnen, Nathalie EG Ligthart, Indrani Chakraborty, Jan Groenewold, Willem K Kegel, Alfons van Blaaderen, and Daniela J Kraft. Conformations and diffusion of flexibly linked colloidal chains. *Journal of Physics: Materials*, 4(3):035002, 2021.

[21] Ruben W Verweij, Julio Melio, Indrani Chakraborty, and Daniela J Kraft. Brownian motion of flexibly linked colloidal rings, 2023.

[22] Angus McMullen, Maitane Muñoz Basagoiti, Zorana Zeravcic, and Jasna Brujic. Self-assembly of emulsion droplets through programmable folding. *Nature*, pages 1–5, 2022.

[23] Gaurav Mitra, Chuan Chang, Angus McMullen, Daniela Puchall, Jasna Brujic, and Glen M Hocky. A coarse-grained simulation model for colloidal self-assembly via explicit mobile binders. *Soft Matter*, 2023.

[24] Carolyn L Phillips, Eric Jankowski, Bhaskar Jyoti Krishnatreya, Kazem V Edmond, Stefano Sacanna, David G Grier, David J Pine, and Sharon C Glotzer. Digital colloids: reconfigurable clusters as high information density elements. *Soft Matter*, 10(38):7468–7479, 2014.

[25] Stefano Angioletti-Uberti, Patrick Varilly, Bortolo M Mognetti, and Daan Frenkel. Mobile linkers on dna-coated colloids: Valency without patches. *Physical Review Letters*, 113(12):128303, 2014.

[26] Bortolo Matteo Mognetti, Pietro Cicuta, and Lorenzo Di Michele. Programmable interactions with biomimetic dna linkers at fluid membranes and interfaces. *Reports on Progress in Physics*, 82(11):116601, 2019.

[27] Tadao Sugimoto and Kazuo Sakata. Preparation of monodisperse pseudocubic α-fe2o3 particles from condensed ferric hydroxide gel. *Journal of Colloid and Interface Science*, 152(2):587–590, 1992.

[28] Yong Wang, Xiaowen Su, Panshuang Ding, Shan Lu, and Huaping Yu. Shape-controlled synthesis of hollow silica colloids. *Langmuir*, 29(37):11575–11581, 2013.

[29] Laura Rossi, Vishal Soni, Douglas J. Ashton, David J. Pine, Albert P. Philipse, Paul M. Chaikin, Marjolein Dijkstra, Stefano Sacanna, and William T. M. Irvine. Shape-sensitive crystallization in colloidal superball fluids. *Proceedings of the National Academy of Sciences*, 112(17):5286–5290, 2015.

[30] Ran Ni, Anjan Prasad Gantapara, Joost De Graaf, René Van Roij, and Marjolein Dijkstra. Phase diagram of colloidal hard superballs: from cubes via spheres to octahedra. *Soft Matter*, 8(34):8826–8834, 2012.

[31] Isaac Torres-Díaz and Michael A Bevan. General potential for anisotropic colloid–surface interactions. *Langmuir*, 33(17):4356–4365, 2017.

[32] John SantaLucia Jr. A unified view of polymer, dumbbell, and oligonucleotide dna nearest-neighbor thermodynamics. *Proceedings of the National Academy of Sciences*, 95(4):1460–1465, 1998.

[33] Lorenzo Di Michele, Bortolo M Mognetti, Taiki Yanagishima, Patrick Varilly, Zachary Ruff, Daan Frenkel, and Erika Eiser. Effect of inert tails on the thermodynamics of dna hybridization. *Journal of the American Chemical Society*, 136(18):6538–6541, 2014.

[34] Patrick Varilly, Stefano Angioletti-Uberti, Bortolo M Mognetti, and Daan Frenkel. A general theory of dna-mediated and other valence-limited colloidal interactions. *The Journal of Chemical Physics*, 137(9):094108, 2012.

[35] Lucia Parolini, Bortolo M Mognetti, Jurij Kotar, Erika Eiser, Pietro Cicuta, and Lorenzo Di Michele. Volume and porosity thermal regulation in lipid mesophases by coupling mobile ligands to soft membranes. *Nature Communications*, 6(1):1–10, 2015.

[36] Christine Linne, Daniele Visco, Stefano Angioletti-Uberti, Liedewij Laan, and Daniela J Kraft. Direct visualization of superselective colloid-surface binding mediated by multivalent interactions. *Proceedings of the National Academy of Sciences*, 118(36):e2106036118, 2021.

[37] Bortolo Matteo Mognetti, ME Leunissen, and Daan Frenkel. Controlling the temperature sensitivity of dna-mediated colloidal interactions through competing linkages. *Soft Matter*, 8(7):2213–2221, 2012.

[38] Stephanie Geggier, Alexander Kotlyar, and Alexander Vologodskii. Temperature dependence of dna persistence length. *Nucleic Acids Research*, 39(4):1419–1426, 2011.

[39] Álvaro González García, Joeri Opdam, and Remco Tuinier. Phase behaviour of colloidal superballs mixed with non-adsorbing polymers. *The European Physical Journal E*, 41:1–15, 2018.

[40] Stefano Angioletti-Uberti, Patrick Varilly, Bortolo M Mognetti, Alexei V Tkachenko, and Daan Frenkel. Communication: A simple analytical formula for the free energy of ligand–receptor-mediated interactions. *The Journal of Chemical Physics*, 138(2):01B401, 2013.

[41] MRW Scheepers, LJ van IJzendoorn, and MWJ Prins. Multivalent weak interactions enhance selectivity of interparticle binding. *Proceedings of the National Academy of Sciences*, 117(37):22690–22697, 2020.

[42] R.W. Verweij. *Anisotropy, multivalency and flexibility-induced effects in colloidal systems*. Leiden Institute of Physics (LION) , Faculty of Science , Leiden University, 2021.

[43] Nicholas B. Schade, Miranda C. Holmes-Cerfon, Elizabeth R. Chen, Dina Aronzon, Jesse W. Collins, Jonathan A. Fan, Federico Capasso, and Vinothan N. Manoharan. Tetrahedral colloidal clusters from random parking of bidisperse spheres. *Physical Review Letters*, 110:148303, 2013.

[44] Yogesh Shelke, Susana Marín-Aguilar, Fabrizio Camerin, Marjolein Dijkstra, and Daniela J Kraft. Exploiting anisotropic particle shape to electrostatically assemble colloidal molecules with high yield and purity. *Journal of Colloid and Interface Science*, 629:322–333, 2023.

[45] Lucia Baldauf, Erin G Teich, Peter Schall, Greg van Anders, and Laura Rossi. Shape and interaction decoupling for colloidal preassembly. *Science Advances*, 8(21):eabm0548, 2022.

[46] Erin G Teich, Greg Van Anders, Daphne Klotsa, Julia Dshemuchadse, and Sharon C Glotzer. Clusters of polyhedra in spherical confinement. *Proceedings of the National Academy of Sciences*, 113(6):E669–E678, 2016.

[47] Fang Lu, Thi Vo, Yugang Zhang, Alex Frenkel, Kevin G. Yager, Sanat Kumar, and Oleg Gang. Unusual packing of soft-shelled nanocubes. *Science Advances*, 5(5):eaaw2399, 2019.

[48] Katherine C Elbert, William Zygmunt, Thi Vo, Corbin M Vara, Daniel J Rosen, Nadia M Krook, Sharon C Glotzer, and Christopher B Murray. Anisotropic nanocrystal shape and ligand design for co-assembly. *Science Advances*, 7(23):eabf9402, 2021.

[49] W Benjamin Rogers and John C Crocker. Direct measurements of dna-mediated colloidal interactions and their quantitative modeling. *Proceedings of the National Academy of Sciences*, 108(38):15687–15692, 2011.

[50] Rémi Dreyfus, Mirjam E Leunissen, Roujie Sha, Alexei Tkachenko, Nadrian C Seeman, David J Pine, and Paul M Chaikin. Aggregation-disaggregation transition of dna-coated colloids: Experiments and theory. *Physical Review E*, 81(4):041404, 2010.

[51] Janna Lowensohn, Bernardo Oyarzún, Guillermo Narváez Paliza, Bortolo M Mognetti, and W Benjamin Rogers. Linker-mediated phase behavior of dna-coated colloids. *Physical Review X*, 9(4):041054, 2019.

[52] Hao Hu, Pablo Sampedro Ruiz, and Ran Ni. Entropy stabilizes floppy crystals of mobile dna-coated colloids. *Physical Review Letters*, 120(4):048003, 2018.

[53] Stephan Jan Bachmann, Marius Petitzon, and Bortolo Matteo Mognetti. Bond formation kinetics affects self-assembly directed by ligand–receptor interactions. *Soft Matter*, 12(47):9585–9592, 2016.

[54] Pritam Kumar Jana and Bortolo Matteo Mognetti. Surface-triggered cascade reactions between dna linkers direct the self-assembly of colloidal crystals of controllable thickness. *Nanoscale*, 11(12):5450–5459, 2019.

[55] Stephan Jan Bachmann, Jurij Kotar, Lucia Parolini, Anela Šarić, Pietro Cicuta, Lorenzo Di Michele, and Bortolo Matteo Mognetti. Melting transition in lipid vesicles functionalised by mobile dna linkers. *Soft Matter*, 12(37):7804–7817, 2016.

[56] Simon Merminod, John R Edison, Huang Fang, Michael F Hagan, and W Benjamin Rogers. Avidity and surface mobility in multivalent ligand–receptor binding. *Nanoscale*, 13(29):12602–12612, 2021.

[57] Stefano Angioletti-Uberti. Understanding the self-assembly of dna-coated colloids via theory and simulations. In *Frontiers of Nanoscience*, volume 13, pages 87–123. 2019.

[58] Frank Smallenburg and Francesco Sciortino. Liquids more stable than crystals in particles with limited valence and flexible bonds. *Nature Physics*, 9(9):554–558, 2013.

[59] Frank Smallenburg, Laura Filion, and Francesco Sciortino. Erasing no-man's land by thermodynamically stabilizing the liquid–liquid transition in tetrahedral particles. *Nature Physics*, 10(9):653–657, 2014.

[60] Kevin L. Kohlstedt and Sharon C. Glotzer. Self-assembly and tunable mechanics of reconfigurable colloidal crystals. *Physical Review E*, 87(3):032305, 2013.

[61] Thomas Gibaud, Edward Barry, Mark J. Zakhary, Mir Henglin, Andrew Ward, Yasheng Yang, Cristina Berciu, Rudolf Oldenbourg, Michael F. Hagan, Daniela Nicastro, Robert B. Meyer, and Zvonimir Dogic. Reconfigurable self-assembly through chiral control of interfacial tension. *Nature*, 481(7381):348–351, 2012.

[62] Chrisy Xiyu Du, Greg van Anders, Richmond S Newman, and Sharon C Glotzer. Shape-driven solid–solid transitions in colloids. *Proceedings of the National Academy of Sciences*, 114(20):E3892–E3899, 2017.

[63] Thomas Gibaud, Edward Barry, Mark J Zakhary, Mir Henglin, Andrew Ward, Yasheng Yang, Cristina Berciu, Rudolf Oldenbourg, Michael F Hagan, Daniela Nicastro, et al. Reconfigurable self-assembly through chiral control of interfacial tension. *Nature*, 481(7381):348–351, 2012.